A Novel Grain-Contact Modelling Approach for Enhanced Petro-Elastic Simulations in Digital Rock Physics Applications

Matthias Halisch[1*], *Arne* Jacob[2], *Olga* Lykhachova[2], *Gordon* Burmester[3]

[1] LIAG-Institute for Applied Geophysics, Stilleweg 2, D-30655 Hannover, Germany
[2] Math2Market GmbH, Richard-Wagner-Straße 1, 67655 Kaiserslautern, Germany
[3] OMV Exploration and Production GmbH, Trabrennstraße 6-8, 1020 Vienna, Austria

Abstract. The characterization of structural and stratigraphic trapping of CO_2 at a given storage site depends primarily on the CO_2 migration in the field. With increased focus on migration-assisted CO_2 sequestration in saline aquifers, CO_2 solubility, residual CO_2 trapping, and process monitoring during CO_2 plume migration are areas of growing research and business interest. CO_2 solubility trapping, a primary drainage process influenced by pressure, temperature, and brine salinity, leads to pH reduction, and promotes reactive geochemical processes. Residual CO_2 trapping, a secondary process as water re-imbibes storage volumes, is equally critical. Both mechanisms are vital for safe storage and form the foundation for cost-efficient monitoring and prediction techniques, leveraging pore-scale rock physics experiments, simulations, and field-upscaling workflows. On the pore scale, computational methods such as pore-network modeling and morphological methods simulate capillary pressure, relative permeability saturation functions, and reactive transport to model CO_2 trapping functions and their evolution over time. This research advances an efficient methodology to characterize rock properties across pore-to-log-to-seismic scales, enabling computation of specific rock physical properties – especially seismic velocities (Vp and Vs) – for dry, variably saturated, and reactive transport-exposed samples. Enhanced grain mineral configuration identification via a watershed segmentation method is central to this approach. By modeling stiffness reduction at grain-grain contact zones and adjusting for contact area, grain size, and surface area, the algorithm overcomes typical overestimations of effective stiffness in standard µ-CT analysis. The presented software developments optimize the need for laboratory measurements, enabling simulation of mixed water-CO_2 saturated storage rocks and their acoustic properties under various conditions. These advancements improve the implementation of seismic 4D monitoring programs, which are often legally required, by facilitating better analysis of physical changes in rock types with time. Furthermore, they enhance understanding of geochemical changes in storage rocks through geomechanical-petrophysical properties, contributing to risk reduction and bolstering social acceptance of CCS projects. By digitally performing necessary measurements and limiting laboratory work to calibration purposes, the environmental compatibility of CCS storage development improves. This study demonstrates the workflow using OMV data, and laboratory measurements on reference and in-situ rock samples from potential CO_2 storage sites.

1 Introduction

The characterization of structural and stratigraphic trapping of CO_2 at a given storage site fundamentally depends on how CO_2 migrates through the subsurface [1]. With increasing interest in migration-assisted CO_2 sequestration in saline aquifers, key areas of research and industry focus include CO_2 solubility, residual trapping, and process monitoring during plume migration.

Solubility trapping, a primary drainage mechanism governed by pressure, temperature, and brine salinity, lowers pH and initiates reactive geochemical processes [2]. Residual trapping, which occurs as formation water re-imbibes the pore space after injection, is equally important [3]. Together, these mechanisms are central to ensuring safe storage and form the basis for cost-effective monitoring and predictive techniques, supported by pore-scale experiments, simulations, and upscaling workflows.

On the pore scale, typical computational approaches such as pore-network modeling and morphological analysis simulate capillary pressure, relative permeability, and reactive transport [4]. These simulations enable the prediction of CO_2 trapping behavior and its temporal evolution. This study builds on a recently developed methodology [5] to characterize rock properties across pore-to-log-to-seismic scales and compute key physical parameters (e.g., compressional and shear wave velocities, Vp and Vs) for dry, variably saturated, and chemically altered rocks.

Corresponding author: matthias.halisch@liag-institut.de

Reactive geochemical processes induced by CO_2 injection can occur both near the wellbore and deeper in the reservoir. Near-wellbore effects - already addressed in earlier studies [6] and ongoing projects [7] - primarily relate to injectivity. Here, episodic injection shows a different behavior than continuous injection, as shown by [8]. During shut-in phases, water saturation may increase due to capillary and gravity-driven flow. In the subsequent injection phase, this leads to higher water mobility compared to continuous injection, potentially promoting more intense mineral dissolution. However, this water may already be close to chemical equilibrium with rapidly dissolving minerals like calcite due to prior contact under high CO_2 partial pressure. As a result, it may have limited additional dissolution capacity. Since carbonate minerals in the investigated samples typically act as cement within the pore network, dissolution could weaken the rock and reduce its mechanical strength. This, in turn, could lower the maximum allowable injection pressure - a key operational concern requiring careful monitoring.

To assess this risk, (digital) core flood tests are proposed to quantify potential weakening caused by carbonate dissolution. While permeability changes can be evaluated directly, the critical question is whether dissolution could also degrade injectivity. In principle, carbonate removal increases porosity and thus may enhance permeability. Yet, downstream re-precipitation is also possible, as super-saturation and evolving thermodynamic conditions may shift the geochemical balance.

Traditional core flooding experiments, especially when combined with rock physics measurements (e.g., Vp/Vs) to track mechanical alterations, are limited in scope due to their complexity and cost. Therefore, digital core flooding is the preferred and more economical approach. It enables a combined analysis of porosity, permeability, and storage efficiency changes over time, including uncertainty quantification and scenario development for CO_2 injection performance.

2 Laboratory Methods

In this section, we briefly introduce the applied mineralogical, petrophysical and imaging techniques that have been utilized for this study.

2.1 Mineralogy

X-Ray Diffraction Analysis. The samples were analyzed by the XRD method to determine the bulk mineralogical composition of the rock samples. We used a Bruker AXS D8 Advance X-ray diffraction spectrometer (copper radiation generated X-ray tube at 40 kV and 40 mA, step size 0.0203792 s per step and X-ray detector Lynxeye XE-T) and the software program DIFRAC.EVA V3 to identify different mineral phases. Sample preparation included grinding to a fine powder in an agate mortar or in a swing mill and placed in a plastic sample holder. The samples had to have a flat upper surface to achieve a random distribution of the lattice orientation. For the quantification of the minerals detected by XRD, the software program TOPAS (Total Pattern Analysis Software) was used. This software is utilizing the Rietveld method based on analytical profile functions and least-squares algorithms to achieve the best fit between a theoretical and a measured pattern.

Thin Section Analysis. Thin section analysis is a specialized and highly informative method used in petrology to study the mineralogical and textural characteristics of rocks at a microscopic level. It involves the preparation of thin slices, typically 30 micrometers thick, from rock specimens, which are then examined under a petrographic microscope. The process begins with the creation of a thin section by impregnating a rock sample with resin and then slicing it to a thickness conducive to translucency. Following this, the thin section is mounted onto a glass slide and ground to achieve the desired thickness. The resulting thin slice is then polished to enhance clarity and facilitate optical analysis, here with a Zeiss Axio light microscope.

2.2 Petrophysics

All samples have been oven dried for 24 h at 105 °C before any ongoing laboratory work took place. Core plugs with 25 mm diameter and 30-40 mm in length have been prepared for the laboratory core analysis. All laboratory experiments were conducted in accordance with the recommended core analysis protocols outlined in [9].

Buoyancy Method. Effective porosity and grain density of the sandstone samples have been determined by the buoyancy method [9]. All samples have been saturated for at least 12h under a high-quality vacuum within a special desiccator. As saturation fluid, degassed brine was used. The fluid density was presumed as constant.

Gas Permeability. Klinkenberg gas permeability was measured (multi-point experiment) using a custom-built steady-state permeameter under ambient conditions (p, T), featuring a special so-called Fancher-type core sleeve. This device was specifically designed for lower overburden pressures (here: 10 bar = 145 psi) to cause less mechanical influence upon brittle and less cemented samples [10], but also features high sealing potential for preventing boundary flow.

Ultrasonic Measurement of Acoustic Velocities. P- and S-wave velocities (Vp and Vs) were determined using a Krautkrämer ultrasonic testing device on both dry and fully brine-saturated sandstone samples. The method is based on measuring the travel time of ultrasonic pulses through cylindrical sandstone core plugs with known lengths. To obtain accurate velocities, the instrument's internal velocity setting was iteratively adjusted until the computed travel time matched the observed signal arrival

time for both compressional and shear waves. This calibration-based approach allows for precise velocity determination, accounting for sample-specific acoustic impedance and transducer coupling conditions. All measurements were performed under ambient laboratory conditions, with careful alignment of the transducers and consistent coupling medium application to ensure reproducibility.

µ-CT Imaging. The 3-D imaging has been performed with a high-resolution X-ray computed tomography (µ-CT) system (nanotom M 180, Baker Hughes Waygate). This device is equipped with a special water-cooled nanofocus X-ray tube (180 kV, 20 W) and a large, water-cooled detector (9 MPx, 12 ms) with a high contrast-to-noise ratio (typically better than 10000:1), available at LIAG (Hannover, Germany). For this study, small samples with diameters of about 8 mm have been cut from the larger core plugs, after the routine core analysis. A resolution of 1.5 µm was chosen to resolve cement bridges and pore throat geometry relevant for mechanical modeling. More details about the scanning procedure can be found amongst others in [11]. The digital image analysis and pore scale modelling was conducted using GeoDict digital rock physics toolbox [12, chapter 4].

3 Sample Material

This study uses Gildehauser (GH) and Berea (BR) Sandstone rock samples as well-known "proxies" as reference material. The Gildehauser sandstone (as the Bentheimer sandstone) originating from the Lower Cretaceous period, is known for its widespread occurrence in northern Germany and the Netherlands. Berea sandstone, on the other hand, is a prominent formation found in Ohio, USA, dating back to the Late Devonian to Early Mississippian periods. These sandstones possess several key features that make them highly suitable for laboratory studies.

They exhibit uniform grain size distribution, with porosity values averaging 24% for GH, and 21% for BR, with good to excellent permeability characteristics, making them ideal candidates for systematic laboratory experiments, e.g., coreflooding or fundamental process characterization. Additionally, their well-defined mineralogical composition allows for precise control and manipulation of experimental parameters, both essential for systematic work in this study.

Besides these references, we use a "live" rock from an OMV CCS candidate site: a clastic sandstone offshore reservoir (denoted as NZ), with variable carbonate cement content, ranging between 2-10%. The sample has been classified in previous in-house (by OMV) sedimentological and petrophysical studies into hydraulic flow units (HFUs). HFUs can be linked through flow zone indexes (FZI) [13] to the drainage and imbibition capillary pressure, and modeled for saturation-height to initial water saturations. The HFU/FZI classification for overall 5 units is aligned with the geological facies model for the OMV CCS candidate site. The sample used in this study originates from HFU2 as shown in Figure 1.

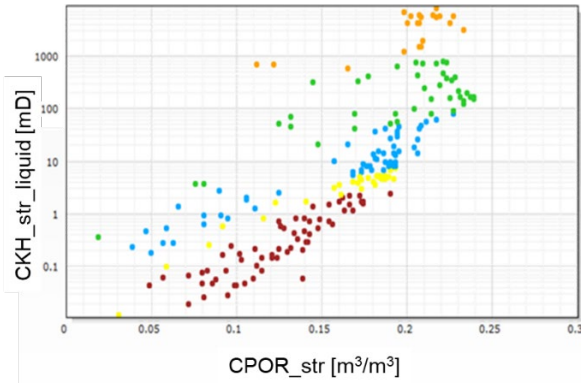

Figure 1. HFU classification (k_w versus porosity) for the OMV CCS candidate site. The sample used for this study originates from HFU2 (green dots).

The porosity for the CCS site sample averages about 19%, i.e., in close range to our reference samples. Nevertheless, due to the carbonate cementation, permeability is lower than for our references. Table 1 provides a comprehensive overview on the basic petrophysical characteristics of our sample material. Subsequently, a detailed mineralogical composition is presented in Table 2.

Table 1. Basic petrophysical characteristics of the rock samples used in this study. "Dry" denotes measured values in dry sample state; "sat" denotes fully brine saturated sample state.

Parameter	GH	BR	NZ
Phi [%]	24	21	19
k [mD]	216	405	155
Vp_dry [m/s]	2856	2486	4197
Vs_dry [m/s]	1531	1629	2061
Vp_sat [m/s]	3546	4200	4804
Vs_sat [m/s]	2544	2650	2926
Vp/Vs (dry)	1.87	1.53	2.04
Vp/Vs (sat)	1.39	1.58	1.64
d [g/cm³]	2.644	2.646	2.610
d_{bulk} [g/cm³]	2.238	2.276	2.304

Table 2. Mineralogical composition of the rock samples used in this study.

Mineral	GH	BR	NZ
Quartz	96 wt.%	82 wt.%	76.5 wt.%
K-feldspar	2 wt.%	6 wt.%	/
Plagioclase	< 1 wt.%	3 wt.%	2 wt.%
Muscovite	/	3 wt.%	/
Pyrite	/	/	8 wt.%
Kaolinite	1 wt.%	6 wt.%	4 wt.%
Calcite	/	/	6.5 wt.%
Dolomite	/	/	3 wt.%

In a new set of in-house petrographic studies by OMV, combining X-ray diffraction and thin section analysis, it was confirmed that the designated reservoir sample contains calcareous pore cement [14], likely to react geochemically during two-phase flow. Complementary multi-mineral log interpretations along the cored well section, and in (cored) offset wells close-by, also confirmed the abundance of calcareous pore cements of up to 10% in the formation of interest [5].

Special emphasis in the core and digital rock calibration is placed on mineral determination that is accessible to CO_2 saturated phases, and related statistical mineral distributions. Thin section analysis (TSA) determined the type of minerals in direct contact to the pore, its abundance, as well as the type of mineral-mineral contacts (e.g., Quartz-Siderite vs. Quartz-Fe-Dolomite) for subsequent calibration of petro-elastic properties.

The petrographic mineral distributions from TSA and XRD are used to guide the manual segmentation process of the digital rock region of interest plug scans as well as drilled sub-plug scans. The manual segmentation ties absolute permeabilities and mineral volumes in the sub-samples and reference plugs, to have a best possible alignment. Additionally, mineral-mineral and mineral-fluid contact faces have been manually picked from thin sections (Figure 2) to validate the contact zones determined by the 3-D image analysis. The pore cement volumes are determined from integrated core (thin section and XRD) and log analysis (Multi-mineral, Quanti ELAN).

4 Digital Rock Physics

Pore scale simulations have been performed with GeoDict, developed and distributed by Math2Market [12]. 3D micro-CT images, derived at a voxel resolution of 1.5 µm have been processed (i.e., filtered & segmented) as described by [15] and cropped to digital volumes with dimensions of 400 x 400 x 400 voxels (i.e., 0.6 mm domain length).

The simulations yield 4-D visualizations of mineral alteration, which are crucial for interpreting the formation of preferential flow paths and the spatial localization of precipitation zones. These effects are particularly important in heterogeneous formations, where local variations in mineralogy and pore geometry significantly affect the global transport behavior.

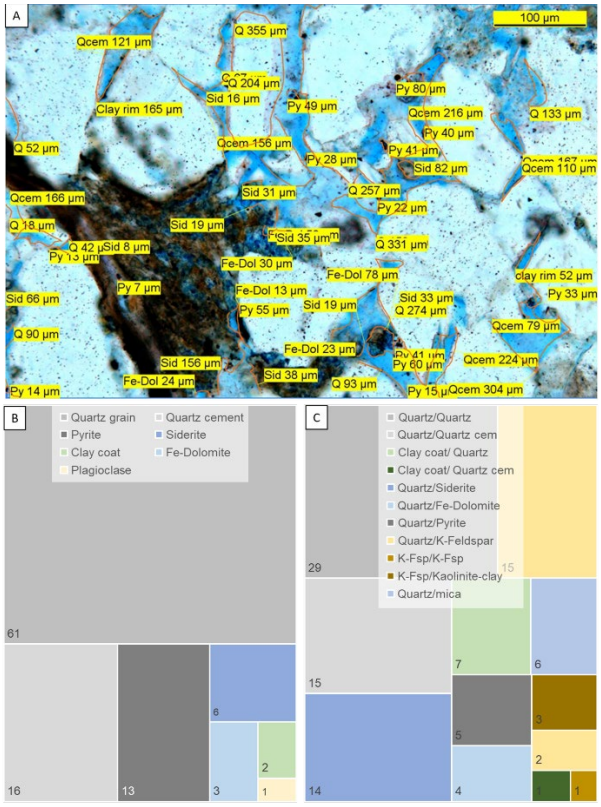

Figure 2. Contact zones manually determined from thin section analysis of the NZ core plug (A), for both, mineral-fluid contact (B), and mineral-mineral contacts (C).

4.1 Mechanical Simulations (Vp / Vs)

As stated, this research aims to develop an efficient methodology to characterize rock properties from pore-to-log-to-seismic scales. Specifically, it focuses on computing the rock physics properties for dry, variably saturated samples, and samples exposed to reactive transport processes.

Our new approach addresses the overestimation of effective stiffness at grain-grain boundaries typically observed in standard µ-CT analysis [16]. Applying GeoDict`s GrainFind Module [17], local grain mineral configurations have been detected by a watershed segmentation algorithm, and is followed by stiffness reduction modeling at grain-grain contact zones. While grain identification, pairs of touching grain fragments are merged or reconnected depending on the interface threshold (in percent), which is calculated as ratio between grain fragment interface and the total surface of the smaller fragment in the pair. The interface threshold influences the number of detected contact surfaces (Figure 3) and, consequently, affects the final stiffness.

This parameter needs to be adjusted individually for each rock, and ideally, verified with thin section-based contact zone measurements. All solid phases are analyzed together, allowing the grains to be treated as multicomponent entities, which minimizes the impact of potential segmentation artifacts.

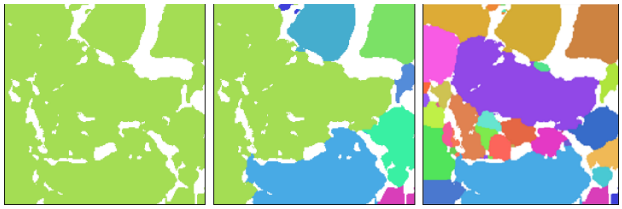

Figure 3. Impact of different interface thresholds in GrainFind. From left to right: 0-5 %, 14 %, 35 %.

By following this procedure, a highly reliable segmentation is achieved, even without using a time and resource demanding registration of the µ-CT images with mineralogical "maps", e.g. derived by scanning electron microscopy. Table 3 summarizes the segmented porosity values and mineral content, respectively.

Table 3. Segmented porosity and mineral content statistics for the three sandstones samples used in this study.

	GH	BR	NZ	E [GPa]
Phi [%]	23.66	22.59	16.30	-
Quartz	75.52	71.43	61.17	95.29
Feldspar	0.616	4.76	10.56	77.71
Calcite	-	0.10	9.66	84.00
Zircon	0.001	-	-	294.86
Illite	0.202	1.12	2.31	67.70

As noted by [18], in a combination with the effects of field of view and solver choice, limited image resolution leads to artificially stiffer elastic properties compared to laboratory measurements. To address this issue, previous approach reduced the number of voxels in segmented contact zones explicitly. In contrast, the current methodology retains the originally segmented voxel geometry and introduces an area-dependent correction factor f to adjust contact stiffness, as a function of relative contact area and grain size. The reduced stiffness assigned to contact voxels is given by:

$$E_{ij} = E_{ii} f \qquad \text{(Eq. 1)}$$

where E_{ii} refers to original stiffness of a grain i: The area-dependent factor f is calculated as:

$$f = f_{\%} f_a \qquad \text{(Eq. 2)}$$

In our case, $f_{\%}$ is a user-defined global coefficient (in percent), assuming a lower stiffness in the contact zones compared to the interior of the grains. It is applied uniformly across all minerals to scale down contact stiffness relative to the original material. The area-based factor f_a is calculated per contact area group within one mineral ID. The defined contact areas are normalized by the maximum contact area, and grouped under the same ID. To meet the limitation of 256 IDs per simulation, they get scaled such that larger contact areas yield a smaller reduction in stiffness (Figure 4).

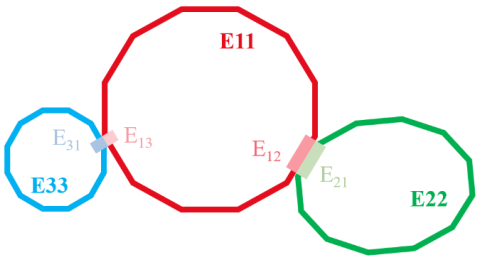

Figure 4. Contact area dependent stiffness ($E_{11} > E_{12} > E_{13}$).

This new approach overcomes the limited image resolution, which causes artificially stiffer elastic properties compared to laboratory measurements as elaborated before. Figure 5 shows the comparison of the initial versus factorized contact zone determination (Fig.5, left hand side) as well as the final segmented structures for the reference samples and the live reservoir rock (Fig.5, right hand side).

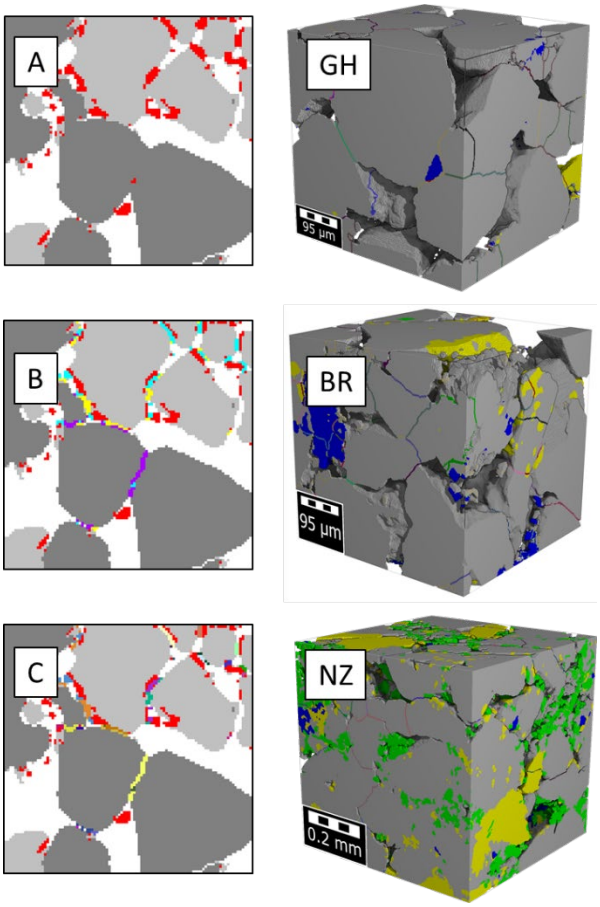

Figure 5. Contact zones, by standard segmentation (A), initial contacts (B) and factorized contacts of one reference sandstone (C) are shown on the left hand side. On the right hand, final segmented structures/grains with marked and factorized contact areas that have been used for the simulations. (Gildehauser = GH; Berea = BR; CCS site = NZ).

The color coding on the left hand side of Fig. 5 depicts basic mineralogy (greyish colors = matrix minerals) and carbonate cement (red). Initial and final factorized contact zones are shown in rainbow colors (Fig. 5B & C). On the right hand side, four mineral phases are segmented for the simulations: grey = quartz, yellow = feldspar, green = cement, blue = clay.

The effective mechanical properties are computed using homogenization method [19] as implemented in the ElastoDict [20]. The module utilizes an iterative Fast-Fourier-Transformation solver [21] to compute the response of a voxelized microstructure subjected to macroscopic strain. The solution involves following system of equilibrium (Eq. 3) and kinematic (Eq. 4) partial differential equations:

$$\nabla \cdot (\sigma(\varepsilon)) = 0 \qquad \text{(Eq. 3)}$$

$$\varepsilon = E + \frac{1}{2}(\nabla u + (\nabla u)^T) \qquad \text{(Eq. 4)}$$

Here, E denotes the macroscopic strain tensor and u the displacement vector. After solving for the local stress σ and strain tensors ε, volume averaging over the 3D domain results to the effective stiffness tensor. Following the mechanical simulation, bulk density and porosity, additional seismic recalculations were executed for each rock sample. Thus, p- and s-wave velocities were derived as follows:

$$v_p = \sqrt{\frac{K + \frac{4}{3}G}{\rho}}, \qquad v_s = \sqrt{\frac{G}{\rho}} \qquad \text{(Eq. 5)}$$

where v_p is the p-wave velocity in m/s, v_s is the s-wave velocity in m/s, K represents the bulk modulus, G is the shear modulus, ρ is the bulk density.

4.2 Reactive Transport Simulations (RTS)

Reactive transport in porous media is a fundamental process underlying numerous subsurface applications, such as geological carbon sequestration, acid stimulation in reservoir engineering, environmental remediation, and underground storage of hydrogen or nuclear waste. These processes involve complex interactions between fluid flow, chemical transport, and mineral reactions, which dynamically alter the porous structure and, consequently, the system's transport properties. Accurate prediction of such feedback mechanisms requires high-resolution modeling tools that can resolve the coupled phenomena at the pore scale. In this study, we employ a physics-based simulation approach using the Reactive Flow GeoApp, part of the GeoDict software suite, to model and analyze mineral dissolution and precipitation under varying flow and geochemical conditions.

The approach is based on coupling Lagrangian transport modeling with thermodynamic equilibrium and kinetic reaction models. We simulate the injection of reactive aqueous fluids (e.g., acidified brine by CO_2 injection) into a 3-D rock geometry derived from micro-CT data. The model tracks individual fluid parcels through the pore space, computing their interaction with the solid phase using either equilibrium thermodynamics (via PhreeqC) or mineral-specific reaction kinetics.

Particle movement is influenced by the drag effect of the fluid flow field. Particles serve as carriers for the invading aqueous phases, while the fluid within the voxels represents the reservoir fluid, which is in equilibrium with both the surrounding rock and itself before the particle carriers are injected. As the simulation progresses, the dissolution process is captured through stepwise updates to the fluid flow, reflecting the continuous interaction between the particles and the reservoir fluid. Each step involves a dynamic exchange, where the fluid of the particles mixes with the reservoir fluid contained within the voxels, allowing for the dissolution and precipitation reactions to occur at the fluid-rock interfaces.

The transport speed of the particles is controlled by the velocity of the invading fluid, which is determined by the pressure gradient within the system. This pressure gradient drives the fluid flow, influencing the rate at which particles are transported through the pore network. Additionally, the local complexity of the pore space plays a significant role in particle movement, as the varying geometry of the pore structure can either facilitate or impede the flow. Areas of high porosity and permeability will allow faster particle transport, while more convoluted or tortuous regions may lead to slower movement.

These interactions between the particles, fluid, and rock are central to the reactive transport model, which captures the complex feedback loops between fluid flow, solute transport, and geochemical reactions, such as mineral dissolution or precipitation. The model simulates how the composition of the fluid changes over time, accounting for both, advective and diffusive transport mechanisms, as well as the effects of chemical reactions on fluid and particle behavior. The movement of particles in the system is governed by a combination of Stokes drag, Brownian motion, and external forces. The Stokes equation is:

$$-\mu \cdot \Delta u + \nabla p = f, \text{ with } \nabla \cdot u = 0 \qquad \text{(Eq. 6)}$$

The equation for particle momentum is:

$$m \cdot dv/dt = 6\pi\mu R/C_a \cdot (u - v + \sqrt{(2D)} \cdot dW(t)/dt) + Q \cdot E + F \qquad \text{(Eq. 7)}$$

Here, m is the particle mass, μ denotes the dynamic viscosity, u is the fluid velocity vector, v is the particle velocity vector, p is the pressure, R is the particle radius, C_a is the Cunningham correction factor, D is the diffusivity accounting for Brownian motion, and f is the force vector. The electrostatic field E is calculated from the electrostatic potential Φ, which is derived by solving

Poisson's equation. The force field F can also include additional external forces, such as gravity or buoyancy, and Q represents the particle charge. These terms can be customized through user-defined functions in the model. The Cunningham correction factor, used to account for reduced drag on very small particles, is given by:

$$C_a = 1 + (\lambda / R) \cdot (1.17 + 0.525 \cdot e^{(-0.78 \cdot R / \lambda)}) \quad \text{(Eq. 8)}$$

The Brownian motion is modeled through the diffusivity:

$$D = k_B \cdot T / \gamma \quad \text{(Eq. 9)}$$

where k_B is the Boltzmann constant, T is the absolute temperature, and γ the friction coefficient, as defined as:

$$\gamma = 6\pi\mu R / C_a \quad \text{(Eq. 10)}$$

In the thermodynamic approach (PhreeqC, Geochemical Equilibrium Thermodynamics), the reaction rates are computed by solving a set of mass action equations for aqueous and mineral species, maintaining charge balance and chemical equilibria at each time step.

Simulation results include the evolution of porosity and permeability, spatial patterns of mineral transformation, and local fluid compositions. The temporal changes in porosity (φ) and permeability (k) can be analyzed to quantify permeability enhancement or reduction due to precipitation-induced clogging or dissolution-driven channel formation.

As part of the research project, a synthetic brine with a total dissolved solids (TDS) content of 50,000 ppm - equivalent to field conditions - was equilibrated with CO_2 under reservoir-representative temperature and pressure. The initial brine, based on field fluid samples, had a pH of 7. For the simulations, this fluid was subsequently replaced by CO_2-equilibrated brine at pH 4 but with identical salinity, and injected over incrementally increasing time periods to enhance the dissolution of grain cement, specifically segmented calcite.

The primary objective was to evaluate the resulting increase in porosity relevant to rock physics trends, rather than to achieve a fully representative model of reactive transport under field-scale conditions. Nevertheless, key simulation parameters - such as an injection rate of 3.5×10^{-6} m/s and a diffusion coefficient of 1×10^{-9} m²/s - were selected in accordance with field measurements to ensure general physical realism (i.e., Péclet number < 1), without aiming to replicate operational dynamics in detail. Derived Damkoehler numbers (see section 5.3) are in accordance with reported literature values [4].

5 Results

5.1 Evaluation of Grain Contact Correction

To validate the improved contact zone modeling methodology, simulations were performed on a test geometry derived from Gildehauser sandstone (GH), using different watershed segmentation reconnect thresholds in GrainFind (35% and 14%) for both the initial and the factorized grain contact models (Figure 6).

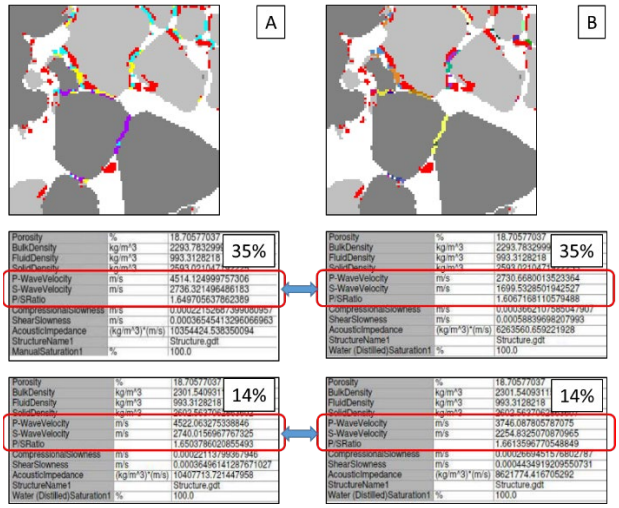

Figure 6. Comparison of different threshold values $f_{\%}$ (35% and 14%) for the detection of grains and according contact zones in GeoDict: (A) for the initially derived contacts from basic watershed segmentation; (B) for the factorized contacts. The influence and the improvements of the contact model on the resulting P- and S-wave values is clearly visible.

In the initial model, which directly derives contact areas from the segmented µ-CT data, no significant changes in acoustic velocities were observed between the two thresholds. For 35%, the simulated values were Vp = 4514 m/s and Vs = 2736 m/s; for 14%, Vp = 4522 m/s and Vs = 2740 m/s. All of these values clearly overestimate the laboratory measurements (compare Table 1, Vp = 3546 m/s, Vs = 2544 m/s), highlighting the systematic stiffness bias in standard segmentation-based contact zone representation.

In contrast, the factorized contact model - which applies an area-dependent stiffness correction - shows a pronounced sensitivity to the threshold variation. For the 35% threshold, Vp = 2730 m/s and Vs = 1699 m/s were obtained; for 14%, Vp = 3746 m/s and Vs = 2254 m/s. The latter values are already in close agreement with the experimentally measured acoustic velocities in the fully saturated state (compare Table 1, Vp = 3546 m/s, Vs = 2544 m/s), demonstrating the accuracy and practical relevance of the new approach.

5.2 Validation of Vp / Vs Simulations

The comparison between simulated and experimentally measured Vp and Vs for both Gildehauser and Berea sandstone samples reveals a differentiated but overall robust performance of the digital rock physics workflow (Table 4). For the Gildehauser sandstone, dry-state simulations show very good agreement with laboratory data for Vp, with a deviation of less than 1%. However, Vs values are significantly overestimated (+22.9%), which may be attributed to an overestimation of shear stiffness at grain contacts in dry conditions. In contrast, the saturated-state simulation yields Vp and Vs values that closely approximate experimental results, with deviations of +8.4% and –5.6%, respectively, and a Vp/Vs ratio closer to the measured data.

For the Berea sandstone, dry-state simulations exhibit larger discrepancies, particularly for Vs (+58.6%) and Vp (+54.2%), indicating that shear and bulk stiffness seem to be over predicted in dry conditions. Nevertheless, the Vp/Vs ratio remains in reasonable agreement. Under saturated conditions, both Vp and Vs simulations achieve excellent correspondence with experimental values (deviations < 5%), underscoring the accuracy of the contact zone model and petro-elastic calibration under saturated reservoir conditions.

Table 4. Comparison of simulation results (indexed "sim") with experimental measurements (indexed "exp"): (A) = Gildehauser Sandstone; (B) = Berea Sandstone.

A. Gildehauser Sandstone				
Parameter	**Phi [%]**	**Vp [m/s]**	**Vs [m/s]**	**Vp/Vs**
dry_{sim}	23.66	2882	1881	1.53
dry_{exp}	24.70	2856	1531	1.87
Δ dry [%]	- 4.21	0.91	22.86	- 18.2
sat_{sim}	23.66	3843	2401	1.60
sat_{exp}	24.70	3546	2544	1.39
Δ sat [%]	- 4.21	8.37	- 5.62	15.11

B. Berea Sandstone				
Parameter	**Phi [%]**	**Vp [m/s]**	**Vs [m/s]**	**Vp/Vs**
dry_{sim}	22.59	3833	2583	1.48
dry_{exp}	22.51	2486	1629	1.53
Δ dry [%]	0.35	54.18	58.56	- 3.27
sat_{sim}	22.59	4264	2765	1.54
sat_{exp}	22.51	4200	2650	1.58
Δ sat [%]	0.35	1.52	4.34	- 2.53

It is acknowledged that the numerical solver exhibits its higher sensitivity and computational demand when simulating dry-state conditions. This is due to the pronounced contrast in elastic moduli and density between solid grains and air, as compared to water-saturated systems. In particular, complex contact topologies involving grain-grain and grain-fluid interfaces tend to increase numerical instability and local errors [19, 21, 22].

Despite these challenges, the dry-state simulation results remain within an acceptable range, especially when accounting for laboratory uncertainties such as signal damping, transducer coupling, and anisotropy effects. The overall performance - especially the good match for saturated conditions according to in-situ measurements (e.g., ± 10% calculated fluid displacement versus log measurement, ± 12% seismic velocity lab measurement) - demonstrates the robustness and predictive capability of the implemented digital rock physics workflow for simulating petro-elastic behavior across a range of reservoir conditions.

5.3 Results of Vp / Vs and RTS on NZ-sample

For the CCS candidate sandstone (NZ), simulated and experimental acoustic velocities show systematic differences, particularly under dry conditions (Table 5, top part). The dry-state simulation yields Vp = 4619 m/s and Vs = 3012 m/s at a porosity of 16.3%, whereas laboratory measurements report Vp = 4197 m/s and Vs = 2061 m/s at 19.05% porosity, resulting in a noticeably higher experimental Vp/Vs ratio (2.04 vs. 1.53). This can be attributed to similar reasons as for the Gildehauser and Berea sandstones.

Under saturated conditions, the agreement improves: simulated values (Vp = 4630 m/s, Vs = 2943 m/s) approach the experimental measurements (Vp = 4804 m/s, Vs = 2926 m/s), with Vp/Vs ratios of 1.57 (sim) and 1.64 (exp). The overall porosity underestimation in simulation is linked to the selection of the 3D geometry from µ-CT data, which in the case of NZ reflects a notably more complex internal composition and heterogeneity compared to the more homogeneous GH and BR samples (compare chapter 3).

Although these differences, the simulated elastic responses follow the expected trends between dry and saturated states, and the overall results for NZ are highly encouraging for further analysis.

Table 5. Comparison of simulation results with experimental measurements, including RTS steps for 1%, 2% and 3% dissolved carbonate cement for the CCS candidate sample.

CCS Candidate (NZ) Sandstone				
Parameter	**Phi [%]**	**Vp [m/s]**	**Vs [m/s]**	**Vp/Vs**
dry_{sim}	16.30	3960	2501	1.58
dry_{exp}	19.05	4197	2061	2.04
sat_{sim}	16.30	4104	2589	1.57
sat_{exp}	19.05	4804	2926	1.64
$dry_{sim\ (RTS\ 1\%)}$	17.26			
$sat_{sim\ (RTS\ 1\%)}$	17.26	4072	2564	1.58
$dry_{sim\ (RTS\ 2\%)}$	18.44			
$sat_{sim\ (RTS\ 2\%)}$	18.44	4416	2795	1.58
$dry_{sim\ (RTS\ 3\%)}$	19.42			
$sat_{sim\ (RTS\ 3\%)}$	19.42	4198	2636	1.59

As part of the reactive transport simulation (RTS) analysis for the CCS candidate sandstone (NZ), preliminary results are available for the 1% carbonate cement dissolution scenario (Table 5, lower part). In this configuration, the simulated porosity increased from 16.30% (initial state) to 17.26%, while the corresponding P- and S-wave velocities under brine-saturated conditions slightly decreased to Vp = 4481 m/s and Vs = 2841 m/s, resulting in a Vp/Vs ratio of 1.58. Compared to the initial saturated simulation (Vp = 4630 m/s, Vs = 2943 m/s), these changes reflect the expected softening of the rock matrix due to early-stage cement dissolution, accompanied by a moderate increase in pore volume.

The magnitude of these acoustic changes is consistent with the progressive increase in porosity and confirms the model's sensitivity to microstructural alterations induced by geochemical reactions. Following the 1% RTS scenario (Φ = 17.26%), simulated velocities under saturated conditions were Vp = 4481 m/s and Vs = 2841 m/s (Vp/Vs = 1.58). With further cement dissolution at 2% and 3% RTS stages, porosity increased to 18.44% and 19.42%, respectively. Corresponding elastic properties decreased gradually, with Vp = 4416 m/s and Vs = 2795 m/s for RTS 2%, and Vp = 4198 m/s and Vs = 2636 m/s for RTS 3%, while Vp/Vs ratios remained nearly constant (~1.58 - 1.59). These results reflect a systematic "weakening" of the rock matrix (i.e., reduction of Young´s modulus) and highlight the ability of the digital approach to capture elastic response evolution under progressive chemical alteration.

The detailed analysis of porosity evolution along the Z-axis of the NZ sample during progressive carbonate dissolution clearly highlights the local variations and intensities of carbonate cement dissolution (Figure 7). Initially, porosity values exhibit noticeable heterogeneity, ranging approximately between 14% and slightly above 20%, reflecting the original distribution of pore space within the sample.

After 1% carbonate dissolution (RTS), a slight yet distinct increase in porosity is observable, confirming the onset of localized carbonate cement removal. These localized increments indicate areas originally enriched in carbonate cement, emphasizing the heterogeneous nature of cement distribution.

Following 2% carbonate dissolution, the porosity increase becomes significantly more pronounced. The porosity distribution distinctly shifts upward, showing well-defined peaks in certain segments of the sample. These segments correspond to areas where higher carbonate cement content has been preferentially dissolved, amplifying the local porosity variations.

With the progression to 3% carbonate dissolution, porosity values achieve substantially higher levels, surpassing initial values markedly, with peak porosity values exceeding 22%. This stage further accentuates previously identified zones, clearly delineating areas with intense carbonate cement dissolution. These regions now represent potential preferential flow paths that could significantly enhance fluid mobility and transport properties in the reservoir.

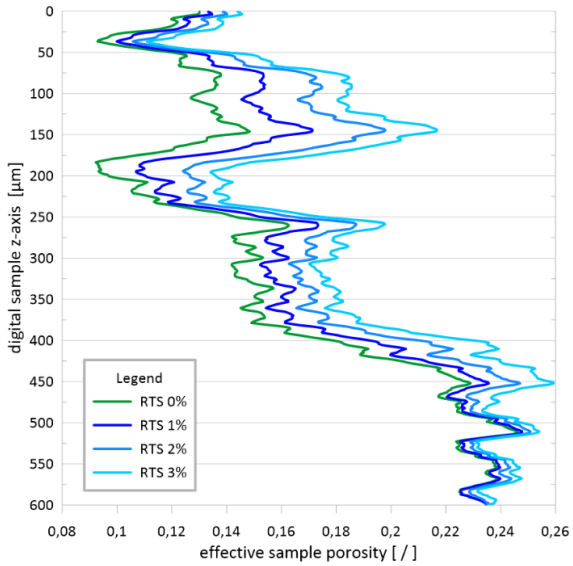

Figure 7. Change in porosity along the sample´s z-axis as derived by the reactive transport simulations: green denotes the initial state, dark blue refers to 1%, blue refers to 2%, light blue to 3% dissolved carbonate cement. Local variations can be linked to areas with stronger and weaker cementation.

Our simulated Damkoehler number (Da1) increased from 4.29 × 10−5 to peak at 5.15 × 10−5, and subsequently decreased to 3.12 × 10−5 over the time of the simulation experiment. We observed a left skewed parabolic trend that indicates a fast increase in pore-cement dissolution, which peaks, while pore cement dissolution slowly decreases over the time of the simulation experiment. A similar value range is reported amongst others in [4]. In line the Da1 variation, the Péclet number starts from 0.62, to drop to 0.61 quickly, subsequently increasing to 0.88 over the time of the simulation. Accordingly, we have not observed any wormhole formation.

Over the scale of a characteristic length, the advective time is smaller than the diffusive time, however, with the increase in pore-cement dissolution, advection slightly increases as wider flow paths (caused by the « uniform » cement dissolution) developed. In summary, the RTS-derived porosity profiles demonstrate a clear, progressive enhancement of porosity correlated directly with increased carbonate cement dissolution. Results provide an impression of affected areas, where the carbonate cement dissolved and flow paths have changed. The non-uniform spatial distribution and varying intensity of porosity increments strongly confirm the heterogeneous nature of carbonate cementation within the studied sample.

Furthermore, these findings underscore the effectiveness and reliability of the RTS modeling approach in realistically capturing mineral dissolution processes.

Capillary pressure and relative permeability were modeled using a combination of pore-scale simulation techniques implemented in the GeoDict software suite, specifically the SatuDict module [17]. Imbibition processes were simulated using a pore morphology method in which capillary pressure decreases monotonically. This approach allows the wetting phase to progressively re-enter pore spaces previously occupied by the non-wetting phase, following the geometry and connectivity of the pore structure. At each saturation state derived from the pore morphology simulation, relative permeability was computed by solving the Stokes equations for incompressible, viscous flow. The phase not under consideration for permeability was treated as a solid, effectively defining the flow domain for the invading or displaced phase. The model incorporates mixed-wettability effects by assigning specific regions of the pore space as non-wettable, thereby preventing wetting-phase invasion in those areas during imbibition. This enables a more realistic representation of fluid displacement behavior in heterogeneous porous media.

GeoDict (spontaneous and forced imbibition) was used to simulate the relative permeabilities, calibrated by existing centrifuge lab experiments (imbibition) presented in [5]. Irreducible water saturations for HFU 2 ranges between 0.12 and 0.28 (0.18 mid-point) from probabilistic petrophysics and rock-fluid database analytics results (in-house) and compares well with simulation results 0.19. Spontaneous imbibition end-points (P_C=0) from centrifuge lab experiments indicate a range between 0.40 and 0.57 for HFU 2, however, probabilistic petrophysical log interpretations in [5] referenced against reservoir saturation tool monitoring (RST) from log data indicate trapped gas saturations between 0.50 and 0.72. The probabilistic wetting settings were adjusted (SVP 50) to accommodate the ranges observed from centrifuge lab experiments and log measurements.

Figure 8 compares drainage (A) and spontaneous/forced imbibition (B) relative permeability curves for the CCS candidate sandstone, before and after 3% carbonate cement dissolution (RTS 3%). Imbibition was simulated by considering mixed-wettability according to [23] on the grain surfaces, where variations in surface energy influenced the capillary forces driving fluid movement, allowing for a more realistic representation of fluid displacement within the porous medium. The trends align well with the previously observed capillary pressure behavior and support the interpretation of increased pore connectivity and reduced capillary constraints due to cement removal.

In Figure 8 (A = Drainage), both the invading gas and displaced brine curves for the RTS 3% condition lie consistently above the corresponding curves in the initial state. This indicates increased mobility for both phases during drainage, which is a typical effect of widened pore throats and reduced capillary entry pressures following cement dissolution. The higher relative permeabilities suggest that the rock allows slightly more efficient phase displacement and flow under drainage conditions, consistent with the lower P_C values observed for RTS 3% in the 0.2–0.6 saturation range.

In Figure 8 (B = Imbibition), the water (invading) phase shows nearly identical relative permeability behavior before and after RTS 3%, suggesting that the wetting-phase pathways remained largely unchanged in terms of flow structure. However, the displaced gas curve for RTS 3% lies significantly above the initial-state curve, indicating that gas mobility remains higher for a longer saturation range, i.e., it is displaced less efficiently during imbibition as the water mobility increases at later point from S_{wi}. This may result from reduced capillary trapping due to increased pore sizes and smoother pore transitions, which decrease snap-off effects and enhance gas connectivity during brine re-entry.

Together, these results confirm that reactive transport processes alter not only elastic and capillary properties but also have quantifiable effects on two-phase flow dynamics. The relative permeability curves reflect a pore network that has become more open and better connected after carbonate cement dissolution - supporting faster drainage and a more gradual, less trapping-prone imbibition process. This is consistent with the capillary pressure versus saturation data observed (but not shown for brevity).

Outlook

Petro-elastic modeling (PEM), which considers both grain-grain contacts [24] and grain-cement interactions [24, 25], provides a powerful framework for inversion and forward modeling of reservoir rock responses. The digital rock technology developed in this study significantly enhances the calibration and predictive capabilities of PEM, ensuring that these models remain closely aligned with core-derived digital rock data. In this context, the grain cement fraction (CCF) and cement cohesion coefficients (CCC), as introduced by [25], represent adjustable parameters that can be effectively tuned to reinterpret existing petro-elastic models and robustly forecast the seismic responses needed for future 4D seismic monitoring campaigns (Figure 9).

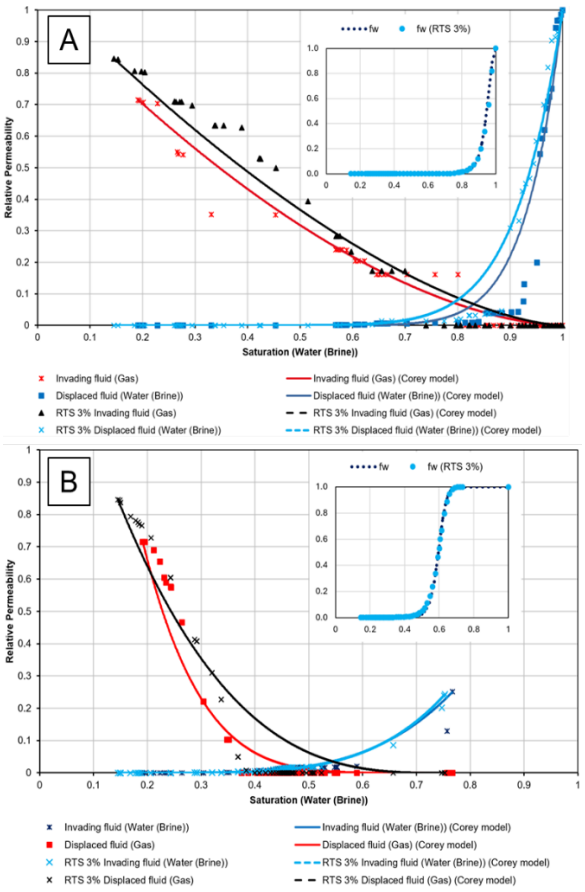

Figure 8. Comparison of drainage (A) and imbibition (B) relative permeability curve from digital rock simulation, before (solid lines) and after (dashed lines) reactive transport simulation (RTS 3%). According fractional flows are shown in the embedded graphs.

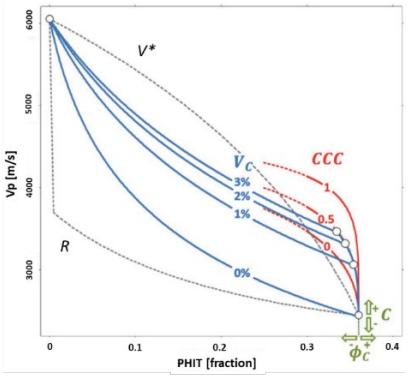

Figure 9. RPT based on the extended cemented sandstone model highlighting the impact of critical porosity (Φ_C), coordination number (C), volume of cement (VC), and CCC on Vp as a function of total porosity, as highlighted in the publication of [25].

The PEM capability is particularly critical for carbon capture and storage (CCS) applications, where accurate tracking and prediction of CO_2 plume migration and trapping efficiency are essential for reservoir integrity, risk management, and regulatory compliance. Figure 11 provides a first impression of this predictive monitoring based upon the CCS candidate reservoir in accordance to the study presented by [25].

Moreover, these advanced PEM approaches are equally valuable for other subsurface reservoir applications beyond CCS. For example, enhanced oil recovery (EOR), underground hydrogen storage (UHS), geothermal reservoir monitoring, and hydrocarbon reservoir depletion studies all benefit from accurate modeling of multiphase fluid interactions and their seismic signatures.

By systematically varying key petro-elastic parameters, realistic scenarios of seismic responses can be generated, supporting optimized reservoir management strategies. These scenarios can either be constructed directly or derived from comprehensive reference databases of rock-fluid interactions and rock physics properties thus enhancing the predictive accuracy and reliability across a wide range of subsurface reservoir management applications.

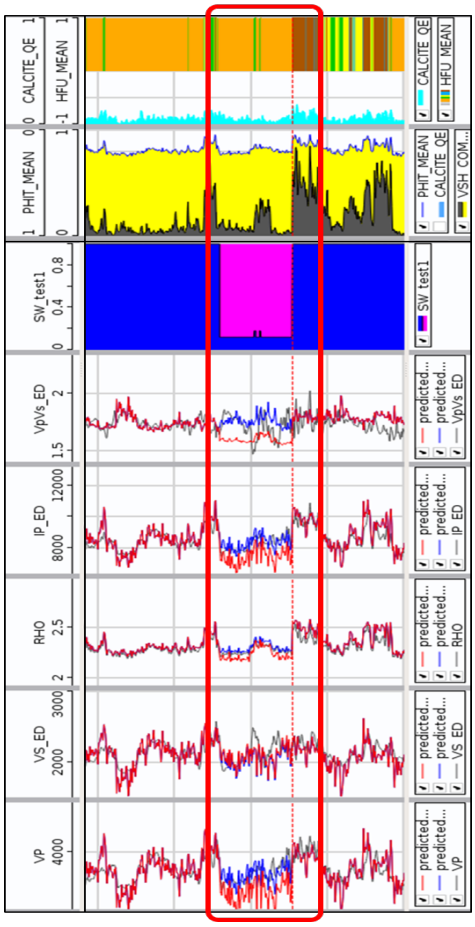

Figure 11. Predictive reservoir simulation using the petro-elastic model showcased in this study. Marked area highlights petrophysical data for $S_w = 1$ (blue) and CO_{2scr} (red) at S_{wi}.

Conclusions

Based on the findings and methodologies presented in this study, the following key conclusions can be drawn regarding the advancements in digital rock physics modeling, petro-elastic simulation accuracy, and their practical implications for CCS and related subsurface reservoir applications:

- A novel grain-contact modeling approach significantly improves petro-elastic simulations by accurately representing grain-grain contacts and grain-cement interfaces derived from µ-CT imaging.
- The developed segmentation method (factorized grain-contact model) effectively corrects the overestimation of stiffness typically observed in standard µ-CT based simulations. Validation on reference sandstones demonstrates good agreement between factorized simulation results and laboratory measurements.
- Sensitivity analyses showed that using different segmentation thresholds significantly affects the simulated elastic velocities in the factorized contact model, highlighting the importance of precise grain-contact characterization. Nonetheless, threshold selection remains a non-trivial task, often relying on the user's petrographic insight and familiarity with microstructural characteristics.
- High-resolution digital rock technology, including µ-CT imaging (1.5 µm voxel resolution), robustly calibrates petro-elastic models, reducing reliance on extensive laboratory measurements.
- Reactive transport simulations (RTS) quantified porosity and permeability evolution due to carbonate cement dissolution under CO_2-rich brine flooding, providing valuable insights for CCS applications. Porosity increased systematically with progressive carbonate cement dissolution (1%, 2%, 3%), directly influencing fluid flow properties and capillary pressure behavior.
- The simulation of 3% carbonate cement dissolution revealed localized porosity increases above 22%, aligning with cement heterogeneity and confirming the model's ability to resolve flow zones and reactive pathways.
- Coupling pore-scale reactive transport and mechanical property simulations enables robust prediction of rock mechanical behavior changes due to mineral dissolution, critically supporting reservoir risk assessment, especially near wellbore regions where dissolution may affect injectivity and storage capacity.
- Relative permeability curves from RTS 3% suggests increased drainage efficiency and reduced wetting-phase trapping, reflecting systematic changes in pore geometry and connectivity.
- The presented digital rock physics workflow significantly enhances the accuracy of seismic monitoring strategies, particularly 4D seismic applications crucial for tracking CO_2 plume migration, improving storage security, and ensuring regulatory compliance.
- The integration of advanced petro-elastic modeling methodologies (adjusting parameters such as grain cement fraction and cement cohesion coefficients) allows the accurate prediction and interpretation of seismic responses in various subsurface reservoir applications beyond CCS, including enhanced oil recovery (EOR), underground hydrogen storage (UHS), geothermal energy extraction, and hydrocarbon reservoir management.

Acknowledgements

The authors would like to acknowledge OMV for permission to publish actual and previous results and data shown in this work. We thank our reviewers of SCA´s Technical Board, Ryan Armstrong and Cyril Caubit, for reviewing and improving this manuscript.

References

[1] S. Benson, Carbon Dioxide Capture and Storage, IPCC Report, 195-277 (2005)

[2] C.A.J. Appelo, D.L. Parkhurst, V.E.A. Post, Geoch. Et Cosmo. Acta, Vol. 125, 49-67 (2014)

[3] C.S. Land, SPE paper, SPE3360, Billings, Mont., 419-425 (1971)

[4] H. P. Menke, B. Bijeljic, M. G. Andrew, M.J. Blunt, Environ. Sci. Technol., 49, 4407-4414 (2015)

[5] G. Burmester, B. Jammernegg, M.A. Garcia Rodriguez, J. Steckhan, H. Ott, EAGE 85th Annu. Conf. Exhib., Extended Abstract, Oslo (2024)

[6] H. Ott, J. Snippe, K. Kloe, Int. J. Greenh. Gas Control, 105 (2021)

[7] B. Jammernegg, K. Heck, D. Martynov, B. Flemisch, H. Ott, EAGE 85th Annu. Conf. Exhib., Oslo (2024)

[8] GOV.UK, Carbon Capture and Storage Knowledge Sharing, Dept. of Energy & Climate Change, link to UK.gov (2016)

[9] API, Recommended Practices for Core Analysis (1998)

[10] M. Rieckmann, Erdöl-Erdgas Z. 36–51 (1970)

[11] M. Halisch, H. Steeb, S. Henkel, C.M. Krawczyk (eds.), Solid Earth 7, 1141–1143 (2016)

[12] Math2Market GmbH, GeoDict 2024, https://doi.org/10.30423/userguide.geodict

[13] J.O. Amaefule, M. Altunbay, D. Tiab, D.G. Kersey, D.K. Keelan, SPE Annu. Tech. Conf. Exhib., Houston (1993)

[14] M. Biernat, F. Zekiri, OMV Tech. Proj. 33243, Report (OMV internal) (2024)

[15] M. Halisch, M. Schmitt, C.P. Fernandes, Int. Symp. Soc. Core Analysts, 1–6 (2016)

[16] H.A. Makse, N. Gland, D.L. Johnson, L.M. Schwartz, Phys. Rev. Lett. 83, 5070 (1999)

[17] A. Blumer, J. Becker, B. Planas, GeoDict 2024 UserGuide: GrainFind Handbook, Math2Market GmbH, Germany, https://doi.org/10.30423/userguide.geodict

[18] N. Saxena, R. Hofmann, A. Hows, E.H. Saenger, L. Duranti, J. Stefani, A. Wiegmann, A. Kerimov, M. Kabel, Geophysics 84(4) (2019) https://doi.org/10.1190/geo2018-0499.1

[19] H. Moulinec, P. Suquet, Comput. Methods Appl. Mech. Eng. 157(1–2), 69–94 (1998) https://doi.org/10.1016/S0045-7825(97)00218-1

[20] L. Burger, S. Rief, A. Widera, B. Planas, GeoDict 2024 UserGuide: ElastoDict Effective Stiffness Handbook, Math2Market GmbH, geodict userguide

[21] H. Grimm-Strele, M. Kabel, Comput. Mech. 64, 1339–1345 (2019) https://doi.org/10.1007/s00466-019-01713-3

[22] M. Kabel, T. Böhlke, M. Schneider, Comput. Mech. 54, 1497–1514 (2014) https://doi.org/10.1007/s00466-014-1071-8

[23] P. Arnold, M. Dragovits, S. Linden, Ch. Hinz, H. Ott, Adv. Wat. Res. Vol. 172, https://doi.org/10.1016/j.advwatres.2023.104381

[24] P. Avseth, T. Mukerji, G. Mavko, Quantitative Seismic Interpretation: Applying Rock Physics Tools to Reduce Interpretation Risk. Cambridge University Press. https://doi.org/10.1017/CBO9780511600074

[25] F. Allo, Lead. Edge 38, 334–340 (2019) https://doi.org/10.1190/tle38050334.1